

## Ultrasound- and microbubble-mediated targeted delivery of therapeutic microRNA-loaded nanocarriers to deep liver and kidney tissues in pigs

Tommaso Di Ianni<sup>1</sup>, Rajendran J.C. Bose<sup>1</sup>, Uday K. Sukumar<sup>1</sup>, Sunitha Bachawal<sup>1</sup>,  
Huajun Wang<sup>1</sup>, Arsenii Telichko<sup>1</sup>, Carl D. Herickhoff<sup>1</sup>, Elise Robinson<sup>1</sup>,  
Sam Baker<sup>2</sup>, José G. Vilches-Moure<sup>2</sup>, Stephen A. Felt<sup>2</sup>, Sanjiv S. Gambhir<sup>1,3</sup>,  
Ramasamy Paulmurugan<sup>1,\*</sup>, Jeremy D. Dahl<sup>1,\*</sup>

1. Department of Radiology, School of Medicine, Stanford University, Stanford, California
2. Department of Comparative Medicine, School of Medicine, Stanford University, Stanford, California
3. Department of Bioengineering, Department of Materials Science and Engineering, Stanford University, Stanford, California

\* These authors contributed equally

### Corresponding Author:

Tommaso Di Ianni  
Department of Radiology  
School of Medicine, Stanford University  
3155 Porter Drive  
Palo Alto, CA 94304  
Email: [todiian@stanford.edu](mailto:todiian@stanford.edu)

## Abstract

In this study, we designed and validated a platform for ultrasound (US) and microbubble (MB)-mediated delivery of FDA-approved pegylated poly lactic-co-glycolic acid (PLGA) nanoparticles (NPs) loaded with anticancer microRNAs (miRNAs) to deep tissues in a pig model. Small RNAs have the ability to reprogram tumor cells and sensitize them to clinically used chemotherapy. However, to overcome their short intravascular circulation half-life and achieve controlled and sustained release into tumor cells, anticancer miRNAs need to be encapsulated into NPs. Moreover, focused US combined with gas-filled MBs provides a safe and noninvasive way to improve the permeability of tumor vasculature and increase the delivery efficiency of drug-loaded nanocarriers. A single handheld, curvilinear US array was used in this study for image-guidance and therapy with clinical-grade SonoVue MBs. First, we validated the platform on phantoms to optimize the MB cavitation dose based on acoustic parameters, including peak negative pressure, pulse length, and pulse repetition frequency. We then tested the system *in vivo* by delivering PLGA-NPs co-loaded with antisense-miRNA-21 and antisense-miRNA-10b in pig liver and kidney. Enhanced miRNA delivery was observed (1.9- to 3.7-fold increase) as a result of the US-MB treatment compared to untreated control regions. Additionally, we used highly fluorescent semiconducting polymer nanoparticles (SPNs) co-delivered with miRNA-loaded PLGA-NPs to visually assess NP delivery. Fluorescent microscopy of SPNs confirmed NP extravasation and showed the presence of particles in the extravascular compartment. Hematoxylin and eosin staining of treated tissues did not reveal tissue damage. The results presented in this manuscript suggest that enhanced delivery of miRNA-loaded NPs to target regions in deep organs is feasible in large animal models using the proposed platform.

## Keywords

Ultrasound, microbubbles, nanoparticles, microRNAs, cancer treatment, targeted drug delivery.

## Introduction

MicroRNAs (miRNAs or miRs) are small, non-coding regulatory molecules responsible for mediating several signaling pathways, which are crucial for cancer initiation and progression, invasion and metastasis, and drug resistance [1]. Abnormal miRNA regulation caused by genetic or epigenetic mechanisms may result in oncogenic effects [2]. Counterbalancing the function of up- or downregulated miRNAs via exogenous manipulation with synthetic sense-miRNA or antisense-miRNA (AmiRNA or AmiR), has shown anticancer treatment effects *in vitro* and *in vivo* [3], [4].

A major challenge of using RNA interference for cancer therapy is the low circulation half-life of naked synthetic small RNAs when they are injected into the bloodstream, which is due to abundant nucleases [5], [6]. A viable strategy to circumvent the rapid intravascular degradation is to shield the miRNAs by enclosing them into nanocarriers [3]. Encapsulation of therapeutic agents into nanoparticles (NPs), including liposomes and polymer or albumin-based NPs, has been extensively investigated in cancer treatment [7]. Importantly, NPs may be designed to enhance the drug biodistribution, accumulation kinetics, and sustained release profile by taking advantage of the tumor enhanced permeability and retention (EPR) effect, i.e. the abnormal permeability of the cancer vasculature that allows larger NPs, which are normally prevented from extravasating, to reach the cancer tissue. This targeted delivery mechanism is particularly interesting as it offers the possibility to increase the therapeutic efficacy of intravenously administered anticancer formulations while minimizing adverse effects in healthy organs due to unintended drug accumulation [8]. Nevertheless, EPR effect-based targeting is highly sensitive to pathophysiological factors like abnormal tumor vascular morphology, variable blood flow rate, and high interstitial fluid pressure, leading to low delivery efficiency and highly heterogeneous drug distribution [9].

Focused ultrasound (US) combined with gas-filled microbubbles (MBs) provides a safe and noninvasive way to increase the tumor vascular permeability through a process named sonoporation [10], [11]. The oscillating US field impinging upon the bubble surface creates stable compressions and expansions at lower acoustic pressures (tens to hundreds of kilopascals) and causes violent MB rupturing if the pressure is strong enough (up to several megapascals). The two phenomena are referred to as stable and inertial cavitation, respectively. MB cavitation promotes the formation of fluid microjets, shockwaves, streaming, and cavitation forces, which in turn give rise to shear stresses on the cellular membrane and vascular barrier. These forces breach the blood vessel walls and facilitate NP extravasation, increasing vascular porosity and hence overcoming the high variability of the EPR effect [12]–[17]. Additionally, focused US enables targeted and controlled drug delivery with high spatial selectivity, as the US-induced effects are spatially limited to the US focus, which can be directed to any desired target region. Previous studies have demonstrated that US and MB therapy is effective to enhance the delivery of large-sized particles or molecules for treatment of a number of diseases including hepatocellular carcinoma [4], non-resectable pancreatic cancer [18]–[20], breast cancer metastasis in the brain [21], and Alzheimer's disease [22].

A system for image-guided US and MB-mediated targeted delivery of miRNA-loaded nanocarriers was implemented and tested in mice by Wang et al. [23], and subsequently used in a longitudinal study investigating the effect of two complementary miRNAs (miR-122 and AmiR-21) combined with doxorubicin in drug-resistant hepatocellular carcinoma [24]. miRNAs were loaded into FDA-approved pegylated poly lactic-co-glycolic acid (PLGA) NPs [25], and US-induced inertial cavitation of circulating MBs was demonstrated to significantly increase the amount of delivered miRNAs and to decrease the tumor growth after repeated cycles of combined therapy [24]. In the current study, we used PLGA-NP co-loaded with AmiR-21 and AmiR-10b, two antisense miRNAs antagonizing the function of endogenous miR-21 and miR-10b, respectively. These miRNAs have been reported to be significantly upregulated in a number of malignancies and to play a role in preventing apoptosis and promoting tumor migration and metastatic spread [1], [26]. Silencing the expression of miR-21 and miR-10b through administration of antagonizing miRNAs was shown to elicit substantial reduction of tumor growth [3].

The objective of this work was to design and validate a platform for targeted delivery of miRNA-loaded NPs to deep tissues in large animal models, as a further step toward clinical translation. In this platform, a single diagnostic US transducer array was used for image-guidance and therapy in combination with clinical-grade SonoVue MBs (Bracco Imaging S.p.A., Milan, Italy). The system was first tested on phantoms to optimize relevant acoustic parameters for maximizing inertial cavitation dose. miRNA-loaded PLGA-NPs were administered systemically in combination with highly fluorescent semiconducting polymer nanoparticles (SPNs), and US treatment was delivered to the liver and kidney of healthy pig models to validate the feasibility of the setup *in vivo*. Uptake of PLGA-NPs was assessed by quantifying the levels of delivered therapeutic miRNAs by quantitative reverse transcription polymerase chain reaction (qRT-PCR), and immunofluorescence (IF) microscopy of SPNs was performed to confirm extravasation of NPs and their presence into the parenchyma.

## Materials and methods

### Delivery platform and ultrasound system

The implemented platform for targeted delivery of miRNA-loaded NPs to deep tissues in large animal models is schematically depicted in **Figure 1A**. MBs and NPs are co-administered intravenously, and MB cavitation, induced by the focused US beam, increases the vascular permeability in the target region and facilitates transport of NPs out of the vascular compartment. The extravasated NPs are then endocytosed by parenchymal cells and release their cargo of miRNA.

A single handheld, curvilinear array transducer (C5-2v; Verasonics Inc., Redmond, WA, USA) was used with a Vantage 256 research scanner (Verasonics Inc.) for image-guided therapy. During the animal experiments, the probe was housed in a custom 3-D printed holder and mounted on a jointed flex-arm stand (Dino-Lite MS-52B; AnMo Electronics Corp., Taipei, Taiwan). The positioning system enables comfortable freehand scanning and allows for probe fixation in the desired target location by locking the arm joints. The

custom holder allows for rotation of the probe in the elevation direction at angular increments of  $2.5^\circ$  (**Figure 1B**).

A B-mode imaging sequence consisting of 13 unfocused emissions steered between  $\pm 9^\circ$  with a center frequency of 4 MHz was used for image guidance (**Figure 1C**) [27], [28]. The beamformed images were displayed with a dynamic range of 60 dB and a frame rate of 6 frames/s. The mechanical index (MI) of the B-mode emissions was 0.15 to avoid nonspecific destruction of bubbles from the imaging pulses.

Therapy was delivered using a focused beam with an F-number of 1.2 and a center frequency of 2 MHz. The emitted acoustic pressure was measured in the XZ and YZ planes with a focus at 70 mm using a needle hydrophone (HNC-0500; Onda, Sunnyvale, CA, USA) in degassed water (**Figure 1D**). The full width at half maximum was 1.9, 2.9, and 21.8 mm in the X, Y, and Z directions, respectively. For calibration, the peak negative pressure was measured with increasing excitation voltage and derated with an attenuation factor of 0.5 dB/(cm MHz).

### Microbubbles

Clinically approved SonoVue contrast agent was used for all the phantom and animal experiments. The MBs consist of a stabilized sulfur hexafluoride gas core surrounded by a phospholipid shell, with diameter in the range of 2 to 9  $\mu\text{m}$  [29]. The contrast agent was resuspended in sterile 0.9% physiological saline and diluted to obtain the desired concentration.

### Phantom experiments

A phantom study was performed to determine the effects of acoustic parameters on the MB cavitation. A concentration of approximately  $10^7$  MB/ml was used. The solution was circulated in a 4-mm diameter flow channel embedded in tissue-mimicking material (Model 527; ATS, Bridgeport, CT, USA) using a flow pump (ISM596D; IDEX, Oak Harbor, WA, USA). A mean velocity of 1.2 mm/s was maintained. The phantom setup is depicted in **Figure 2A**. The US probe was positioned at a distance of 70 mm from the vessel, and a focused US beam was used to induce MB cavitation. Peak negative pressure, pulse length, and pulse repetition frequency (PRF) of the therapy pulse were varied as reported in **Figure 2B**. Two hundred pulses were delivered for each set of acoustic parameters.

To measure the inertial cavitation dose (ICD), the broadband emission generated by inertial cavitation events was detected by using the same transducer array. The root mean square (RMS) intensity of the recorded echoes was calculated (over the frequency range  $5.5 \text{ MHz} \pm 150 \text{ kHz}$ ) and integrated over the number of delivered pulses. The measurement was first performed on a saline-filled vessel to estimate the baseline noise floor, and then repeated with circulating MBs. The baseline noise floor was then subtracted from the RMS intensity resulting from MB cavitation to obtain the ICD [30]. The data processing and ICD calculation were performed in MATLAB (The MathWorks, Inc., Natick, MA, USA).

Analysis of variance (ANOVA) was used to assess the presence of a significant effect of each parameter on the measured ICD. A Wilcoxon signed-rank test was used for pairwise comparisons within



each set of acoustic parameters. All statistical tests were performed in RStudio 1.1.442, and statistical significance was considered for  $p < 0.05$ .

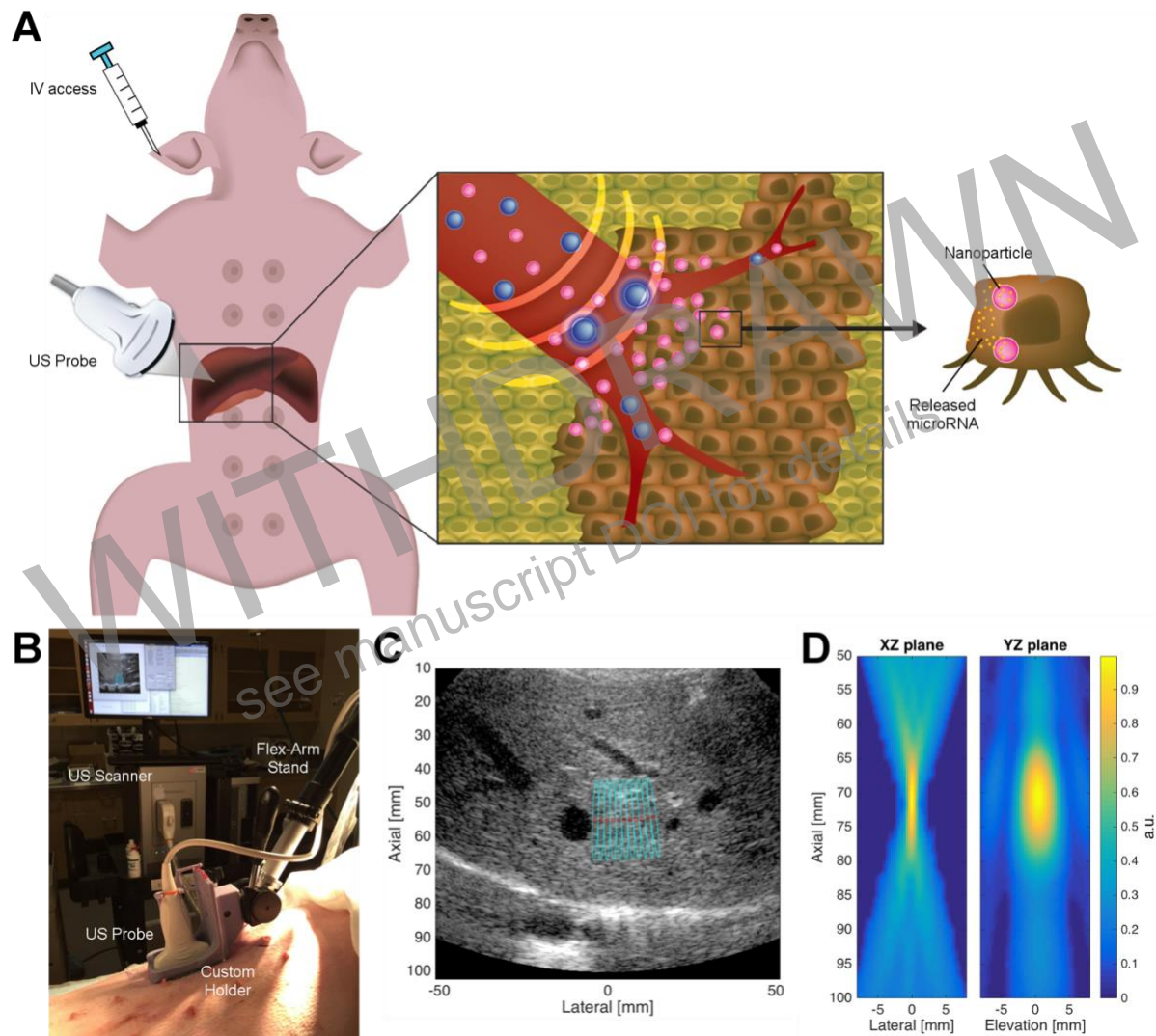


**Figure 1.** (A) Schematic representation of the ultrasound-mediated drug delivery platform. MBs (blue) and NPs (pink) are co-administered intravenously and circulate in the blood pool (red). MBs cavitating under the effect of a focused US beam increase the vascular permeability facilitating NP extravasation. The NPs are then endocytosed and release their miRNA cargo. (B) Picture of the setup during an animal experiment. The image shows the US probe mounted on the flex-arm stand. (C) B-mode image of the pig liver used for therapy guidance. The US therapy focal regions are overlaid and depicted in cyan. (D) Hydrophone measurements of the focused US beam in the lateral (XZ) and elevation (YZ) planes.

## Nanoparticle synthesis

### *AmiR-21 and AmiR-10b-loaded PLGA-NPs*

PLGA-NPs loaded with AmiR-21 and AmiR-10b were prepared using a double emulsion solvent evaporation technique as described previously [3], [23]. In brief, the miRNAs (10 nmol) were complexed

with spermidine in an N/P ratio of 15:1 in DNase/RNAase free water for 15 min at room temperature. The miRNA-spermidine complex was added dropwise to the stirred solution of FDA-approved pegylated PLGA polymer (10 mg) dissolved in dichloromethane (DCM, 1 ml) containing 3% Span-80. Successively, the complex was sonicated for 60 sec at 40% amplitude (SFX-150; Branson Ultrasonics, Danbury, CT, USA) in an ice bath to form the first emulsion. The mixture was added to 5 ml of emulsifying water (Tween-80, 1% w/v) and sonicated at 40% amplitude in an ice bath for 60 sec to form the second emulsion, followed by stirring for 3 h to facilitate evaporation of the DCM. The NPs were then sterile filtered using a 0.45- $\mu$ m syringe filter (Whatman PURADISC 25 AS; GE Healthcare Life Sciences, Pittsburg, PA, USA). Excess surfactants and free miRNAs were removed by centrifuging the NPs three times in sterile DNase/RNAase free water (Invitrogen, Grand Island, NY, USA) at 3000 rpm using an ultracentrifuge filter device with 100 kDa MWCO Membrane (Amicon Ultra; Merk Millipore, Burlington, MA, USA). The size and Zeta-potential of the PLGA-NPs were measured using a Zetasizer Nano ZS90 sizing device (Malvern Panalytical Ltd., Malvern, U.K.). NP concentration was quantified with nanoparticle tracking analysis (NTA) by NanoSight NS300 (Malvern) using 10 mg of PLGA dissolved in 3.3 ml of deionized water. Gel electrophoresis was used to determine encapsulation and loading efficiency of miRNAs after extracting the loaded miRNAs from a fixed amount of NPs, as well as from the washed solution.

#### *SPNs*

SPNs are fluorescent NPs made of organic and biocompatible polymer material with high brightness and controllable dimensions. We synthesized these particles with characteristics similar to the PLGA-NPs and used them as a model nanocarrier to confirm NP extravasation via IF confocal microscopy. SPNs were prepared following a protocol described previously [31] with minor modifications. Briefly, 15 mg of 1,2-Distearoyl-sn-glycero-3-phosphoethanolamine-N-[methoxy(polyethyleneglycol)-2000] (ammonium salt; DSPE-mPEG) were dissolved into 1 ml of DCM solution containing 0.25 mg/ml of poly[2,7-(9,9-dioctylfluorene)-alt-4,7-bis(thiophen-2-yl)benzothiadiazole] (PFODBT). The mixture was poured into distilled-deionized water (10 mL) under continuous sonication with an ultrasonic sonifier (Branson Ultrasonics) at a power output of 6 W RMS for 10 min on ice. DCM was evaporated at 45°C under nitrogen atmosphere. Finally, the aqueous solution of SPNs was filtered through a 0.22  $\mu$ m polyvinylidene fluoride membrane filter, and particle concentration was quantified by NTA.

#### **Animal preparation**

The experimental protocol for the animal study was approved by the Institutional Animal Care and Use Committee at Stanford University. The university's animal care and use program and facilities are AAALAC International accredited, PHS-assured, and USDA licensed. Healthy female Yorkshire pigs (Pork Power Farms, Turlock, CA; weight range: 28-32 kg) were used in this study. The animals were fed a commercially prepared balanced ration ad libitum (Nature's Match Sow & Pig Complete, Purina Mills LLC, St Louis, MO)

and fasted overnight prior to the compound administration and imaging procedure. Reverse-osmosis water delivered through both an automatic watering system and in a bowl was made available at all times.

The animals were anesthetized with intramuscularly administered tiletamine HCL and zolazepam HCL (8 mg/kg; Telazol; Pfizer, New York, NY, USA), intubated, and kept under inhalant 2-4% isoflurane in oxygen (2 l/min). Vascular access was created via an intravenous catheter inserted in the marginal ear vein. Pigs were administered acetylsalicylic acid (Aspirin; Wedgewood, Swedesboro, NJ, USA) intravenously (3.5 mg/kg) 5 min prior to NP injection. Vital signs including heart rate, respiratory rate, blood pressure, oxygen saturation, end-tidal CO<sub>2</sub> pressure, EKG, and body temperature were monitored during the entire procedure with an anesthesia and monitoring system (SurgiVet, Dublin, OH, USA).

### **Drug delivery protocol**

Prior to the therapy procedure, the liver and right kidney were imaged from a subcostal view. Easily-accessible regions were identified in the two organs at a depth of approximately 70 mm, and the two imaging windows were marked on the skin. A solution of PLGA-NPs co-loaded with AmiR-21 and AmiR-10b (8 ml;  $8 \times 10^{11}$  NP/ml) and SPNs (3 ml;  $5.13 \times 10^{13}$  NP/ml) was administered with a bolus injection. A volume of 25 ml SonoVue was diluted with sterile 0.9% saline in a 40-ml solution. The MB solution was continuously infused at a rate of 16.67  $\mu$ l/s for the entire duration of the therapy procedure (approximately 40 min).

Focused US treatment was initiated 2 min after the MB infusion was started to ensure a steady state of MB perfusion. The treatment was performed first in the liver and subsequently in the right kidney. A 10-cycle focused US pulse was used for drug delivery with a derated in-situ peak negative pressure of 5.3 MPa ( $MI = 3.8$ ;  $I_{spta} = 26.4$  mW/cm<sup>2</sup>), based on the optimized system parameters from the phantom experiments. Eleven therapy foci were used in each plane, with a lateral displacement equal to the measured lateral FWHM (**Figure 1C**). The probe was rotated over 10 angular positions to cover a therapy volume of approximately  $20 \times 20 \times 27.5$  mm<sup>3</sup>. For each therapy region, eight hundred pulses were delivered with a PRF of 4 Hz.

### ***In vivo* experiments and tissue collection**

We preliminarily tested the US platform in two animals to validate US imaging parameters and probe positioning to target liver and kidney. It was not possible to analyze tissues from these animals due to the inability to identify the therapy regions at necropsy, as discussed below.

A third animal was anesthetized, administered an injection of miRNA-loaded PLGA-NPs, and recovered following anesthesia. The pig was re-anesthetized 24 h later and euthanized by means of injection of pentobarbital sodium (Beuthanasia-D; Schering-Plough Animal Health, Union, NJ, USA). Tissue was collected from the liver, lung, heart, spleen, and pancreas for miRNA quantification to evaluate the drug biodistribution 24 h post NP injection.

A fourth animal received NP administration followed by US treatment with MB infusion. An US-guided injection of 300  $\mu$ l Matrigel (BD Matrigel Matrix Phenol Red-Free; BD Biosciences, San José, CA, USA)



mixed with indocyanine green (ICG; Intrace Medical SA, Lausanne, Switzerland) dye was performed adjacent to the target area to facilitate its identification *ex vivo* by optical imaging. The animal was kept under anesthesia until euthanasia 4 h post NP injection. The liver was resected and imaged with an IVIS Spectrum (PerkinElmer, Chicago, IL, USA) scanner to locate the targeted area marked by the Matrigel-embedded ICG dye. Liver tissue was collected from the treated region and from a distal end of the organ (untreated) that was not influenced by the US treatment. Samples were collected from the right (treated) and left (untreated) kidney. In addition, samples of lung, heart, spleen, and pancreas were harvested for miRNA quantification to evaluate the drug biodistribution 4 h post NP injection.

A liver tissue sample was obtained from a fifth animal that did not receive any injection or US treatment. This sample was used for a baseline quantification of endogenous miRNA (miR-122) and considered as a negative control.

### **MicroRNA quantification**

Harvested samples for miRNA quantification were snap-frozen on dry ice immediately after resection. The levels of delivered therapeutic AmiR-21 and AmiR-10b were evaluated by using qRT-PCR. Samples of tissue of 100 mg were homogenized using a PRO250 tissue homogenizer (PRO Scientific, Oxford, CT, USA) in 300  $\mu$ l lysis buffer for 3 min. Total RNA (mRNA and miRNA) was isolated from the lysates using mirVana miRNA Isolation Kit (Life Technologies, Grand Island, NY, USA) adopting the total RNA extraction procedure according to the manufacturer's protocol.

For miRNA quantification, 50 ng of total RNA was reverse transcribed using RT-primers (Life Technologies) for AmiR-21 and AmiR-10b using a custom ordered TaqMan kit and a microRNA Reverse Transcription Kit (Life Technologies). RT-PCR was performed using cDNA (5 ng equivalent of total RNA) combined with TaqMan RT-PCR reagents (primer and probe mix) of AmiR-21 and AmiR-10b. qRT-PCR was performed by 2 min incubation at 50 °C followed by activation of the DNA polymerase at 95 °C for 10 min, 60 cycles of 95 °C for 15 sec, and 60 °C for 60 sec in a Bio-Rad CFX96 Touch™ Real-Time PCR Detection System (Bio-Rad, Hercules, CA). The presence of AmiR-21 and AmiR-10b was calculated using the  $2^{-\Delta CT}$  method [32]. The RT-PCR quantification was repeated three times for each analyzed sample. The miRNA levels were normalized to the endogenous level of miR-122 in a control liver sample from the animal that was administered neither NPs nor US and MB therapy.

### **Immunofluorescence staining**

Tissue samples for IF analysis were fixed in 4% paraformaldehyde overnight at 4 °C, immersed in a 30% sucrose solution for cryoprotection, and frozen at -80 °C. Tissues were then embedded in optimal cutting temperature media (OCT; Fisher Scientific, Whitby, Ontario, Canada) and cryosectioned in slices of 10  $\mu$ m thickness. The sections were stained for F-actin (using phalloidin) and vascular endothelial cell marker CD31 for visualizing the cytoskeleton and blood vessels, respectively.

The slices were rinsed in phosphate-buffered saline (PBS) for 10 min, permeabilized in 0.5% Triton-X 100 in PBS, and incubated in a blocking solution of 3% bovine serum albumin (Sigma, St. Louis, MO, USA), 3% normal goat serum (Sigma), and 3% normal donkey serum (Sigma) for 60 min at room temperature. The samples were then incubated with a rabbit-anti-human CD31 primary antibody (1:100; Abcam, Cambridge, MA, USA) at 4 °C overnight in a humidifying chamber. Samples were then incubated with a goat anti-rabbit Alexa Fluor 488 IgG secondary antibody (1:250; Invitrogen) and Alexa Fluor 633-phalloidin (1:100; Invitrogen) for 30 min. Samples were mounted in aqueous mounting media (BiogeneX, San Ramon, CA, USA) and imaged with a LSM710 metaconfocal microscope (Carl Zeiss GmbH, Jena, Germany) at 20X magnification. A tiled confocal micrograph was obtained using a motorized staged controlled by the microscope acquisition software (AxioVision; Carl Zeiss). Image analysis was performed in Fiji 2.0.0 [33].

### Hematoxylin and eosin staining

Kidney and liver samples were fixed in 10% neutral buffered formalin at room temperature, routinely processed, embedded in paraffin, and sectioned with a microtome into 5 µm thick slices for routine hematoxylin and eosin (H&E) staining. Tissue assessment was performed blindly by a veterinary pathologist (JGVM).

## Results

### Inertial cavitation dose measurement in phantom

The results of the ICD measurements in phantom with varying acoustic parameters are reported in **Figure 2C, 2D, and 2E**. In each plot, the ICD was normalized to the mean ICD for the lowest value of each parameter, i.e. peak negative pressure of 0.13 MPa, pulse length of 2 cycles, and PRF of 1 Hz.

The ICD was significantly influenced by all the parameters tested (ANOVA;  $p < 0.0001$ ). Peak negative pressure and pulse length had the highest effect on cavitation, with a 33- and 38-fold maximum increase for the pressure and pulse length, respectively. A plateau was reached for pressure above 2.57 MPa (**Figure 2C**), and no statistical difference was found between 2.57, 3.85, and 5.34 MPa ( $p = 0.89$  for 2.57 and 3.85;  $p = 0.71$  for 2.57 and 5.34;  $n = 4$ ). Similarly, there was no statistical significance between pulse lengths of 5, 10, and 20 cycles (**Figure 2D**;  $p = 0.312$  for 5 and 10;  $p = 0.061$  for 5 and 20;  $n = 4$ ). Conversely, the PRF caused a decreasing trend on the measured ICD, although the difference was minimal (< 2-fold maximum decrease). No statistical significance was found between 4, 10, and 20 Hz (**Figure 2E**;  $p = 0.216$  for 4 and 10;  $p = 0.112$  for 4 and 20;  $n = 4$ ).

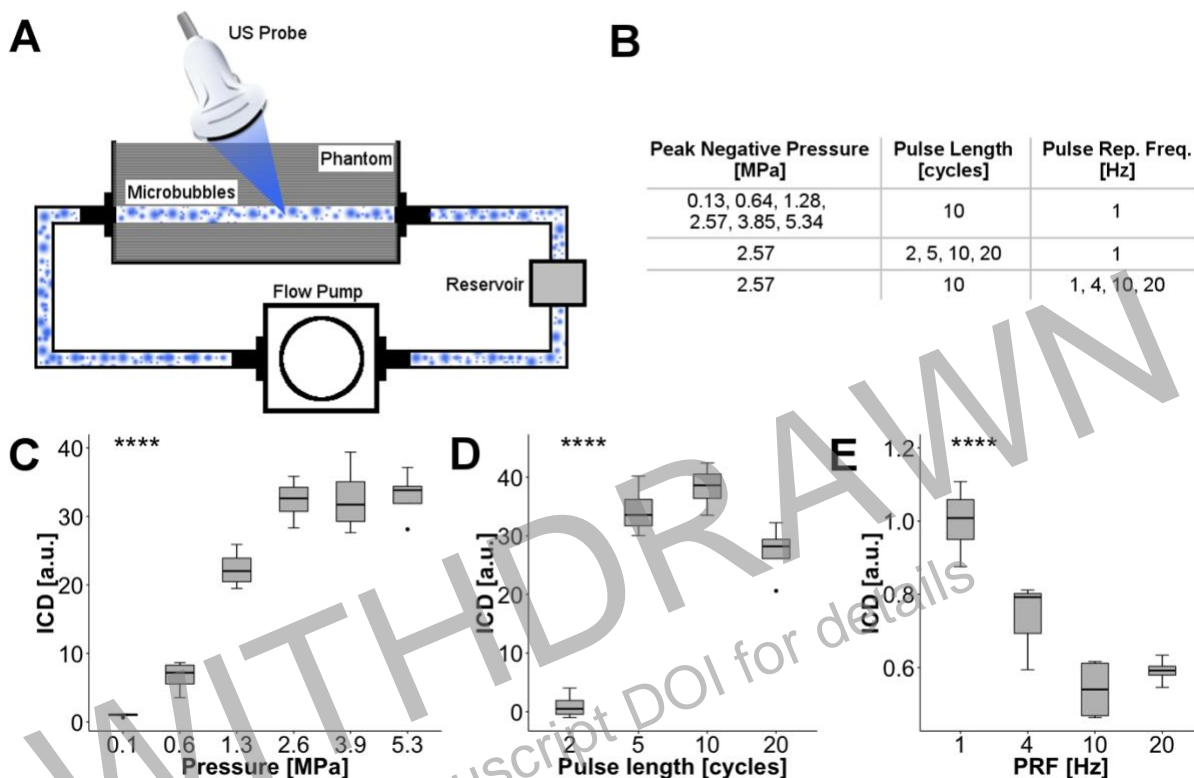


**Figure 2.** (A) Schematic representation of the phantom setup used for assessing the effect of varying acoustic parameters on the measured ICD. (B) Parameters tested in the phantom study. (C, D, E) Box plots showing the effect of peak negative pressure, pulse length, and pulse repetition frequency on the MB cavitation. The ICD was significantly influenced by all the tested parameters (ANOVA). A plateau-like behavior was observed, with no statistical difference between pressures of 2.57, 3.85, and 5.34 MPa, pulse lengths of 5, 10, and 20 cycles, and PRF of 4, 10, and 20 Hz (n = 4). \*\*\*\*: p < 0.0001 (ANOVA).

## Nanoparticle characterization

### *AmiR-21 and AmiR-10b-loaded PLGA-NPs*

Particle characterization results are reported in **Figure 3**. The hydrophilic surfactant Tween 80 (hydrophilic/lipophilic balance (HLB) = 15) and lipophilic surfactant Span 80 (HLB = 4.3) was used as emulsifier and spermidine was used as a counter ion for the encapsulation of AmiRs. Dynamic light scattering (DLS) analysis confirmed that formulated PLGA-NPs were below 150 nm in size with homogeneous size distribution (polydispersity index (PDI) < 0.25; **Figure 3C**). The zeta potential of PLGA-NPs was in the range -20 to -40 mV (**Figure 3D**), likely due to the anionic nature of antisense-miRNA incorporated in the NPs. The average size and Zeta-potential of PLGA-NPs were  $115.3 \pm 18$  nm and  $-32.2 \pm 2.8$  mV, respectively. The final particle concentration quantified by NTA was  $3.3 \times 10^{12}$  NP/ml (**Figure 3B**). The miRNA encapsulation efficiency was analyzed using organic/aqueous extraction method and was equal to  $60.1 \pm 5.3\%$ .

Size and shape of PLGA-NPs were further confirmed by transmission electron microscopy with phosphotungstic acid as negative staining. The loading efficiency of antisense-miRNAs in PLGA-NPs was

quantified by optical CCD camera imaging for the loaded Cy5-AmiR-21 after resolving the NPs by agarose gel electrophoresis. The average number of antisense-miRNAs encapsulated in various NP formulations was estimated to be in the range of 600 to 1000 molecules/NP. The results indicate that co-loading of AmiR-21 and AmiR-10b in PLGA-NPs is found almost at equimolar concentration in NPs prepared in different batches. The antisense-miRNAs extracted from the equimolar mixture of NPs formulated with each antisense-miRNAs (AmiR-21 and AmiR-10b) separately was used as control.

### SPNs

Coprecipitation of PFODBT and DSPE-mPEG in water yielded highly fluorescent SPNs. During NP formation, the hydrophobic lipid tails of DSPE-mPEG, driven by their strong hydrophobic interaction, should be embedded into the NPs, while the PEG-linked DSPE head should extend into the aqueous environment. DLS analysis confirmed that SPNs have a narrow size distribution with a PDI of 0.17. The zeta potentials of SPNs were measured to be  $-32.2 \pm 2.8$  mV in ultrapure water (**Figure 3D**). The average size of SPNs was  $116 \pm 5$  nm (**Figure 3C**). The maximum excitation/emission wavelength was 523/630 nm. The data reveal that the presence of DSPE-mPEG slightly affects the size of SPNs but increases their zeta potential, possibly yielding improved aqueous stability.

To test the *in vitro* cell-labelling efficiency of SPNs, breast cancer cell lines (SKBR3 and MDA-MB-231) were used as a model. After incubation of cells with SPNs at a concentration of 50  $\mu$ g/ml at 37 °C for 8 h, live cells were imaged by fluorescence microscopy (**Figure 3E**). Bright red fluorescence of SPN clusters was located in the cytoplasm rather than limited to the cell membrane, indicating uptake by the cells.

### Delivery of AmiR-21 and AmiR-10b-loaded PLGA-NPs

RT-PCR quantification of exogenous AmiR-21 and AmiR-10b delivered to liver and kidney in the treated pigs is reported in **Figure 4** along with the biodistribution at 4 h and 24 h time points. The miRNA levels are normalized to the level of endogenous miR-122 in the liver of a negative control animal that received neither NP injection nor US treatment. The levels of AmiR-21 in the liver (**Figure 4A**) increased 991-fold in response to PLGA-NP injection alone (untreated region) and 1884-fold after US and MB therapy (treated region), compared to the control animal. The level of AmiR-10b in the liver increased 89-fold due to NP injection and 245-fold post US treatment, compared to the control animal. Therefore, US and MB-mediated delivery yielded a 1.9- and 2.7-fold increase of the two exogenous miRNAs in liver. Levels of AmiR-21 quantified in the kidney (**Figure 4B**) increased 160-fold due to NP injection and 598-fold in response to US treatment, while the levels of AmiR-10b increased 15- and 42-fold for the two cases. Hence, the increase due to US and MB treatment was 3.7- and 2.8-fold for the two exogenous miRNAs in the kidney.

The biodistribution of AmiR-21 in **Figure 4C** (log scale) shows an overall decrease of exogenous miRNA in the liver, kidney, and heart at 24 h compared to the 4 h time point. In contrast, the level of delivered AmiR-21 increased substantially at 24 h in the lung and spleen (36- and 6-fold, respectively).

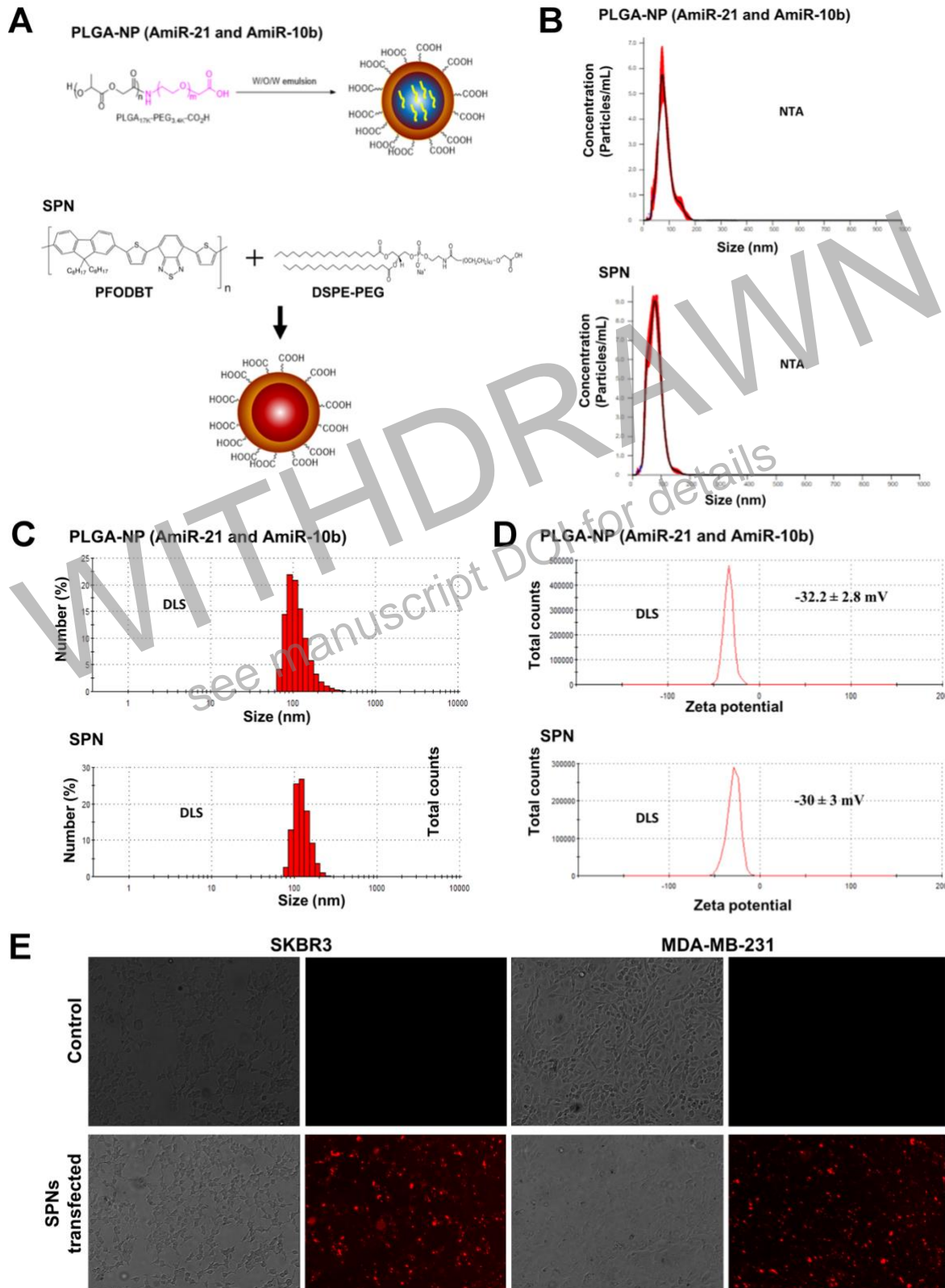


**Figure 3.** Nanoparticle preparation and characterization. (A) Schematic illustration of PLGA-NPs (top) and SPNs (bottom). (B) Particle concentration quantified through NTA. (C, D) Particle size distribution and zeta potential quantified by DLS. (E) Brightfield (left) and confocal fluorescent microscope (right) images of SKBR3 and MDA-MB-231 cell lines with (bottom) and without (top) incubation with SPNs.



## Immunofluorescence analysis

To confirm that increased level of exogenous miRNA was due to enhanced delivery of PLGA-NPs in response to the US and MB-mediated therapy, we performed IF confocal microscopy of SPNs as a model system to mimic the miRNA-loaded PLGA-NPs. Representative IF images are shown in **Figure 5** for both a treated (**Figure 5A**) and untreated (**Figure 5B**) liver region. The IF images confirmed presence of SPNs in the liver parenchyma and in regions peripheral blood vessels, indicating extravasation. Increased presence of SPNs was also noticed in the treated liver sample with respect to the untreated region, although we did not perform a quantitative assessment of the fluorescence levels due to the unequal distribution of the IF signal in various tissue region.

## Histological analysis

Representative H&E-stained sections of pig liver and kidney tissues are shown in **Figure 6**, for the treated and untreated regions. The stained samples were examined to detect changes such as hemorrhage, inflammation, and edema.

The liver and kidney samples that received US-MB treatment had no evidence of hemorrhage, inflammation, or edema attributable to the experimental treatment. Mild sinusoidal distention was observed in numerous lobules in both treated and untreated liver samples. The condition was globally present throughout the liver and was deemed to result from a preexisting condition, and not due to the US-MB treatment. Overall, the US-MB treatment did not cause tissue damage in the liver or kidney after 4 h from the therapy administration.

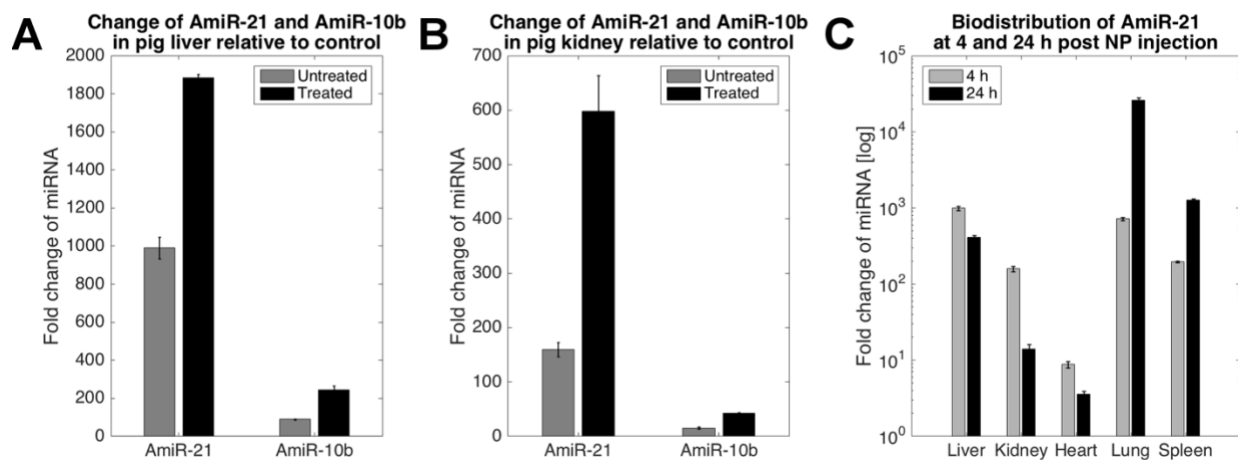


**Figure 4.** RT-PCR quantification of exogenously delivered AmiR-21 and AmiR-10b. The miRNA levels are expressed as fold changes relative to expression of miR-122 in the liver and kidney of a negative control animal that was administered neither drug-loaded PLGA-NPs nor US and MB therapy. Results are reported as mean and standard deviation of the three RT-PCR quantifications. **(A)** Levels of AmiR-21 and AmiR-10b in pig liver in an untreated region and in the area treated with US and MB therapy. **(B)** Levels of AmiR-21 and AmiR-10b in pig kidney in the untreated region and in the area treated with US and MB therapy. **(C)** Biodistribution of AmiR-21 at 4 h and 24 h after injection of miRNA-loaded PLGA-NPs.

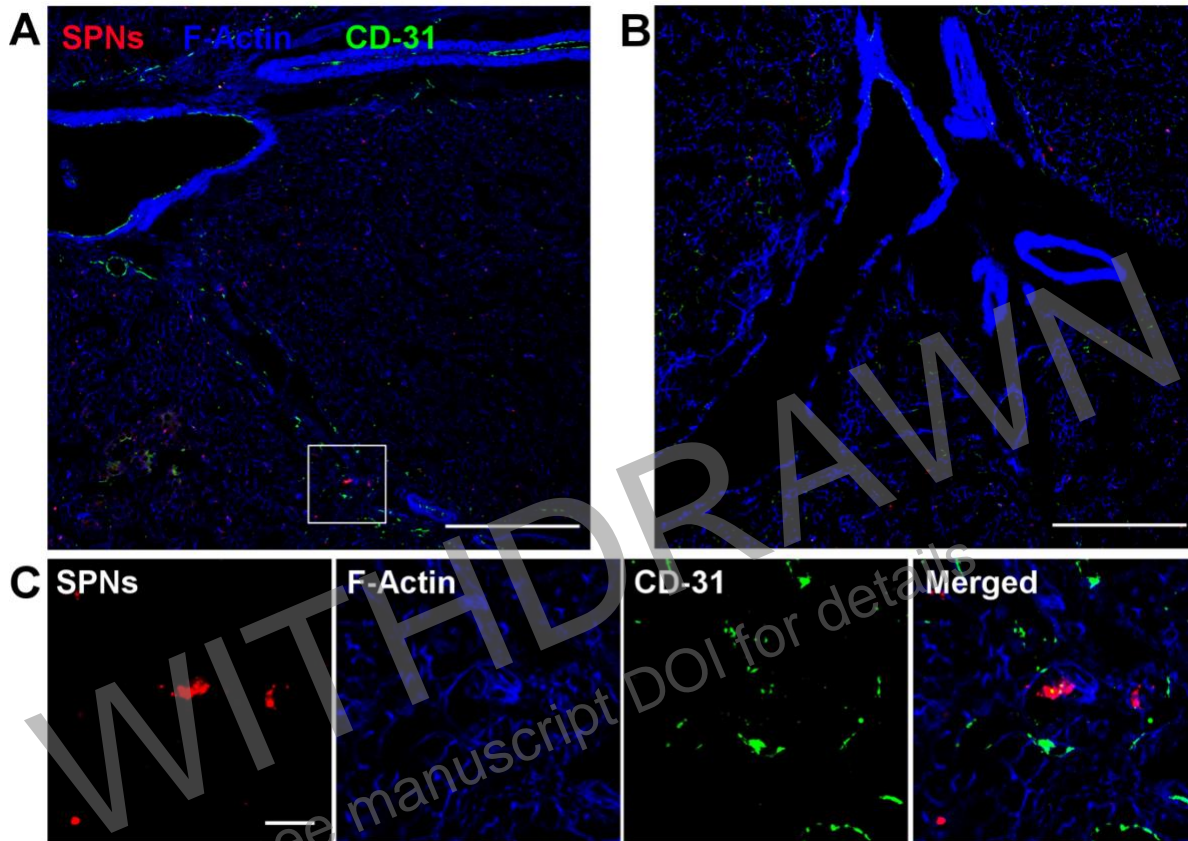


**Figure 5.** Representative immunofluorescence images of SPN model drug (red) in pig liver. The samples were stained for endothelial marker CD31 (green) and F-actin (blue) for cytoskeleton visualization. (A) Treated region in pig liver. (B) Untreated region in pig liver. (C) Magnification of region inside the square in (A) reported for split and merged channels. Scale bar: 200  $\mu\text{m}$  in (A) and (B); 20  $\mu\text{m}$  in (C).

## Discussion

In this study, we reported the design and validation of a platform for US and MB-mediated targeted delivery of FDA-approved PLGA-NPs loaded with anticancer miR-21 and miR-10b in a large animal model. The results showed enhanced miRNA delivery in the liver and kidney, with an increase in quantified miRNA levels of 1.9- to 3.7-fold due to the US-MB treatment. Notably, extravasation of NPs was confirmed through IF microscopy of co-delivered SPNs as a model nanocarrier, showing the presence of fluorescent particles in the extravascular compartment. In addition, H&E analysis did not show tissue damage in the treated organs, confirming the safety of the approach.

Focused US combined with US-sensitive MBs has been previously used in a number of preclinical applications in large animal models. Dewitte et al. delivered mRNA to lymph nodes in dogs through destruction of drug-loaded MBs [34]. Similarly, Liu et al. used MBs loaded with miR-21 as delivery vectors for cardiac gene transfection in pigs [35]. Importantly, US therapy was recently used in clinical trials combined with drug-loaded MBs to investigate its feasibility in the treatment of pancreatic or liver cancer patients [19], [36]. Here, we use PLGA-NPs as a delivery vector rather than encapsulating the therapeutic



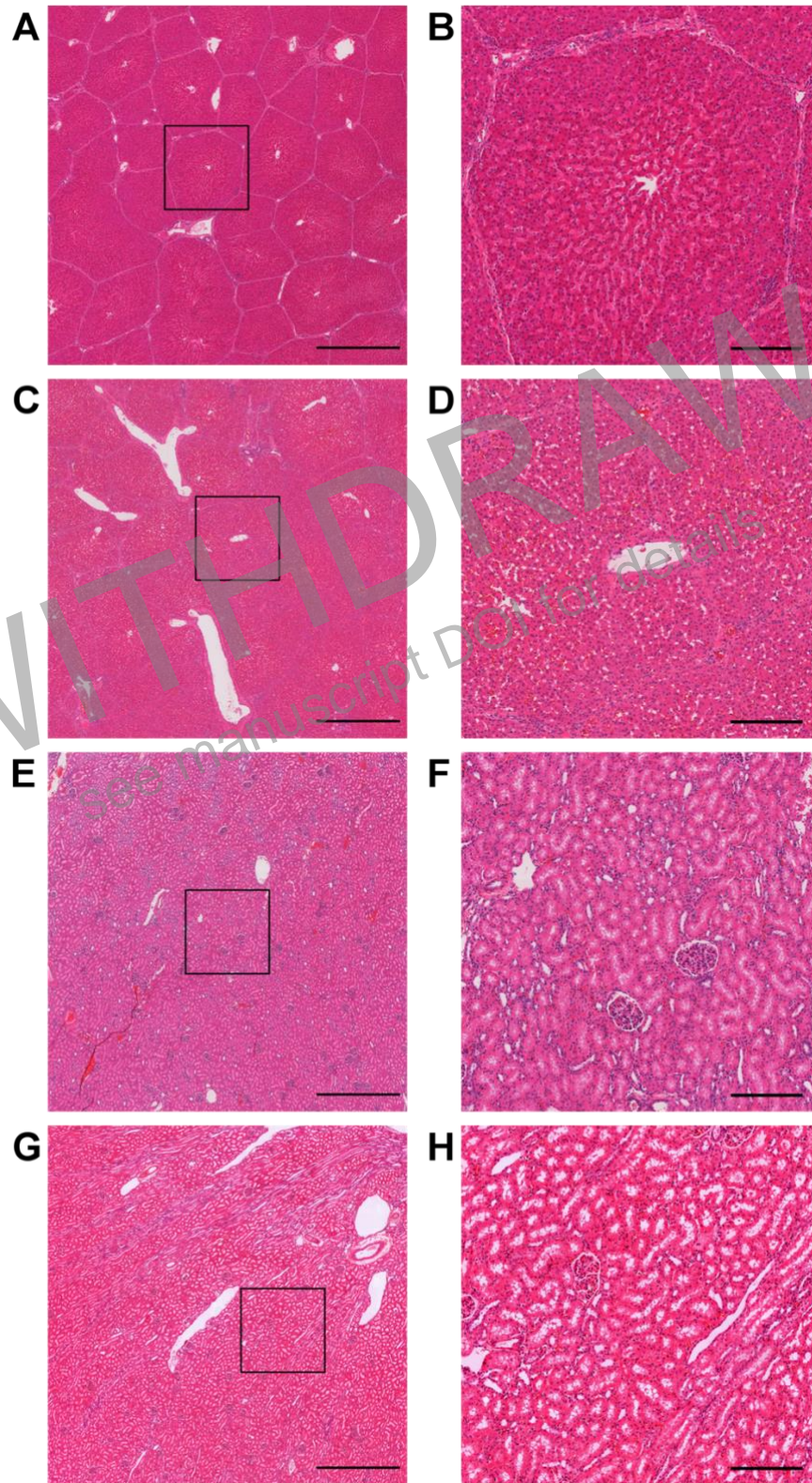


**Figure 6.** Representative H&E images of pig tissue. Liver samples for treated and untreated regions are shown in (A) and (C), respectively. Kidney samples for treated and untreated regions are shown in (E) and (G), respectively. (B), (D), (F), and (H) show magnification of the areas inside the black square in (A), (C), (E), and (G), respectively. Scale bar: 1 mm in (A), (C), (E), (G); 200  $\mu$ m in (B), (D), (F), (H).

miRNAs directly into the MBs to increase the miRNA circulation half-life and improve the drug release profile. To the best of our knowledge, this is the first study demonstrating a platform for US-mediated delivery of miRNA-loaded PLGA-NPs to deep tissues (70 mm) in large animals.

The objective of our study was to translate the drug delivery platform that we previously designed and tested in mice [23] for use in large animal models, as a further step toward clinical translation. The platform was implemented on a commercially available scanner using a single curved array transducer for image-guided therapy and with clinical-grade MBs. We chose a pig model to test our system *in vivo* primarily because of anatomical similarities with humans, in particular with respect to the position and depth of liver and kidney, and due to our prior expertise with this animal model. However, it was important to determine if sufficient inertial cavitation of circulating MBs could be achieved at depth by using a diagnostic ultrasound transducer. Therefore, we first performed a phantom study to optimize the relevant acoustic parameters for maximizing ICD. The optimized parameters were then used for the *in vivo* experiments. We observed a plateau-like behavior for the measured ICD at higher pressure, pulse length, and PRF. A possible explanation for this effect is that MBs were destroyed in a larger volume and/or faster while not being replenished quickly enough to increase the ICD. However, this situation is not reflective of the behavior *in vivo*, where MBs are replenished through a more complex vasculature.

RT-PCR quantification showed a 1.9- and 2.7-fold increase in the liver and 3.7- and 2.8-fold increase in the kidney for exogenous AmiR-21 and AmiR-10b, respectively. The results are comparable to the amount of miRNA quantified in hepatocellular carcinoma xenografts in mice after US treatment [23]. miRNA levels were overall higher in the liver due to clearance of the NPs in this organ. We show that at 24 h there is decreased exogenous AmiR-21 in the liver, kidney, and heart with respect to the level at 4 h, while the miRNA level increased substantially at 24 h in the lung and spleen. This may be due to the uptake of PLGA-NPs by immune cells, which accumulate in these organs. To confirm the presence of NPs in the liver parenchyma, we performed IF microscopy of SPNs. Importantly, the SPNs were located peripherally to the endothelial marker CD31, supporting the hypothesis of transvascular transport and entry of NPs in the extravascular compartment.

We acknowledge the presence of several limitations in our experimental design. First, a single animal was used for quantification of delivered miRNA in the target regions, therefore we could not demonstrate reproducibility of the results. However, we observed a similar delivery effect in two different organs (kidney and liver) within the same animal. Additionally, the delivered antisense miRNAs are not available in the animal system under normal conditions, hence the observed variations may not be attributable to other endogenous confounding factors. We performed the treatment on a total of four animals. The first three pigs received US therapy in the liver only and were euthanized 24 h post NP administration. We performed an US-guided injection of India ink immediately after the treatment to mark the targeted region and facilitate its identification *ex vivo*. However, we could not find traces of dye at necropsy and were unable to locate the treated area in the liver, possibly due to the fast clearance of ink from the organ. For this reason, we modified the experimental protocol to euthanize the fourth pig at 4 h post NP administration. We kept the

animal under anesthesia for the whole duration of the treatment to avoid significant organ displacement and injected a solution of Matrigel with ICG dye. The Matrigel solution solidifies immediately at 37 °C becoming a gelatinous matrix that is not quickly cleared by the liver. In the kidney, we targeted the lower pole to facilitate localization based on the anatomy of the organ.

A second limitation of our study was that only healthy animals were used, due to the challenges of producing a cancer model in pigs. Our future work will focus on delivering miRNA-loaded PLGA-NPs in client-owned dogs with advanced liver cancer. While we expect increased levels of delivered miRNAs in cancer compared with healthy tissue due to the more fragile and leakier tumor vasculature, challenges may arise from hypovascularized or necrotic regions preventing circulating MBs and NPs to reach the target area.

Finally, our current implementation did not include measurement of cavitation signals during the administration of US therapy *in vivo*. Future implementations will include real-time cavitation monitoring to ensure optimal sonication conditions over the treatment period.

In conclusion, through this study we show the design and validation of a single-probe US platform for targeted delivery of miRNA-loaded PLGA-NPs to deep organs in large animal models. The implemented platform represents a step further toward translation of this targeted drug delivery system in humans.

### Abbreviations

AmiRNA or AmiR: antisense-microRNA; ANOVA: analysis of variance; DCM: dichloromethane; DLS: dynamic light scattering; DSPE-mPEG: 1,2-Distearoyl-sn-glycero-3-phosphoethanolamine-N-[methoxy(polyethyleneglycol)-2000]; EPR: enhanced permeability and retention; FWHM: full width at half maximum; H&E: hematoxylin and eosin; HLB: hydrophilic/lipophilic balance; ICD: inertial cavitation dose; ICG: indocyanine green; IF: immunofluorescence; MB: microbubble; MI: mechanical index; mRNA: messenger RNA; miRNA or miR: microRNA; NP: nanoparticle; NTA: nanoparticle tracking analysis; PBS: phosphate buffered saline; PDI: polydispersity index; PFODBT: poly[2,7-(9,9-dioctylfluorene)-alt-4,7-bis(thiophen-2-yl)benzothiadiazole]; PLGA: poly lactic-co-glycolic acid; PRF: pulse repetition frequency; qRT-PCR: quantitative reverse transcription polymerase chain reaction; RMS: root mean square; SPN: semiconducting polymer nanoparticle; US: ultrasound.

### Acknowledgements

This work is dedicated to the memory of Dr. Juergen K. Willmann, whose mind laid the foundations of this project. We thank Amy Thomas for assistance with the illustrations, Dr. Andrew Olson and the Stanford Neuroscience Microscopy Service for assistance with the confocal microscopy, and the Stanford Animal Histology Services for preparation of brightfield histology. This work was supported by the Focused Ultrasound Foundation and the National Institutes of Health (grants numbers R01CA209888 and R21EB022298). The Stanford Neuroscience Microscopy Service is supported by grant NIH NS069375.



## Declaration of Interest

None.

## References

- [1] G. A. Calin and C. M. Croce, "MicroRNA signatures in human cancers," *Nat. Rev. Cancer*, vol. 6, pp. 857–866, 2006.
- [2] C. M. Croce, "Causes and consequences of microRNA dysregulation in cancer," *Nat. Rev. Genet.*, vol. 10, pp. 704–714, 2009.
- [3] R. Devulapally *et al.*, "Polymer Nanoparticles Mediated Codelivery of AntimiR-10b and AntimiR-21 for Achieving Triple Negative Breast Cancer Therapy," *ACS Nano*, vol. 9, no. 3, pp. 2290–2302, 2015.
- [4] S. M. Chowdhury *et al.*, "Ultrasound-guided therapeutic modulation of hepatocellular carcinoma using complementary microRNAs," *J. Control. Release*, vol. 238, pp. 272–280, 2016.
- [5] P. S. Mitchell *et al.*, "Circulating microRNAs as stable blood-based markers for cancer detection," *Proc. Natl. Acad. Sci. U.S.A.*, vol. 105, no. 30, pp. 10513–10518, 2008.
- [6] C. V. Pectot, G. A. Calin, R. L. Coleman, G. Lopez-Berestein, and A. K. Sood, "RNA interference in the clinic: challenges and future directions," *Nat. Rev. Cancer*, vol. 11, pp. 59–67, 2011.
- [7] R. K. Jain and T. Stylianopoulos, "Delivering nanomedicine to solid tumors," *Nat. Rev. Clin. Oncol.*, vol. 7, no. 11, pp. 653–664, 2010.
- [8] T. M. Allen and P. R. Cullis, "Drug Delivery Systems: Entering the Mainstream," *Science (80)*, vol. 303, pp. 1818–1822, 2004.
- [9] Y. H. Bae and K. Park, "Targeted drug delivery to tumors: Myths, reality and possibility," *J. Control. Release*, vol. 153, no. 3, pp. 198–205, 2011.
- [10] K. Ferrara, R. Pollard, and Mark Borden, "Ultrasound Microbubble Contrast Agents: Fundamentals and Application to Gene and Drug Delivery," *Annu. Rev. Biomed. Eng.*, vol. 9, pp. 415–47, 2007.
- [11] S. Hernot and A. L. Klibanov, "Microbubbles in ultrasound-triggered drug and gene delivery," *Adv. Drug Deliv. Rev.*, vol. 60, pp. 1153–1166, 2008.
- [12] L. C. Phillips, A. L. Klibanov, B. R. Wamhoff, and J. A. Hossack, "Targeted gene transfection from microbubbles into vascular smooth muscle cells using focused, ultrasound-mediated delivery," *Ultrasound Med. Biol.*, vol. 36, no. 9, pp. 1470–1480, 2010.
- [13] A. F. H. Lum, M. A. Borden, P. A. Dayton, D. E. Kruse, S. I. Simon, and K. W. Ferrara, "Ultrasound radiation force enables targeted deposition of model drug carriers loaded on microbubbles," *J. Control. Release*, vol. 111, pp. 128–134, 2006.
- [14] P. Marmottant and S. Hilgenfeldt, "Controlled vesicle deformation and lysis by single oscillating bubbles," *Nature*, vol. 423, pp. 153–156, 2003.
- [15] P. Prentice, A. Cuschieri, K. Dholakia, M. Prausnitz, and P. Campbell, "Membrane disruption by optically controlled microbubble cavitation," *Nat. Phys.*, vol. 1, pp. 107–110, 2005.
- [16] A. van Wamel *et al.*, "Vibrating microbubbles poking individual cells: Drug transfer into cells via sonoporation," *J. Control. Release*, vol. 112, pp. 149–155, 2006.
- [17] C.-D. Ohl *et al.*, "Sonoporation from Jetting Cavitation Bubbles," *Biophys. J.*, vol. 91, pp. 4285–4295, 2006.
- [18] S. Kotopoulos *et al.*, "Sonoporation-Enhanced Chemotherapy Significantly Reduces Primary Tumour Burden in an Orthotopic Pancreatic Cancer Xenograft," *Mol. Imaging Biol.*, vol. 16, pp. 53–62, 2014.
- [19] G. Dimcevski *et al.*, "A human clinical trial using ultrasound and microbubbles to enhance gemcitabine treatment of inoperable pancreatic cancer," *J. Control. Release*, vol. 243, pp. 172–181, 2016.
- [20] H. Nesbitt *et al.*, "Gemcitabine loaded microbubbles for targeted chemo-sonodynamic therapy of pancreatic cancer," *J. Control. Release*, vol. 279, pp. 8–16, 2018.
- [21] M. Kinoshita, N. McDannold, F. A. Jolesz, and K. Hynynen, "Noninvasive localized delivery of Herceptin to the mouse brain by {MRI-guided} focused ultrasound-induced blood–brain barrier disruption," *Proc. Natl. Acad. Sci.*, vol. 103, no. 31, pp. 11719–11723, 2006.

- [22] N. Lipsman *et al.*, “Blood–brain barrier opening in Alzheimer’s disease using MR-guided focused ultrasound,” *Nat. Commun.*, vol. 9, p. 2336, 2018.
- [23] T.-Y. Wang *et al.*, “Ultrasound-guided delivery of microRNA loaded nanoparticles into cancer,” *J. Control. Release*, vol. 203, pp. 99–108, 2015.
- [24] S. M. Chowdhury *et al.*, “Longitudinal assessment of ultrasound-guided complementary microRNA therapy of hepatocellular carcinoma,” *J. Control. Release*, vol. 281, pp. 19–28, 2018.
- [25] R. Devulapally and R. Paulmurugan, “Polymer nanoparticles for drug and small silencing RNA delivery to treat cancers of different phenotypes,” *Wiley Interdiscip. Rev. Nanomed. Nanobiotechnol.*, vol. 6, pp. 40–60, 2013.
- [26] R. Garzon, G. A. Calin, and C. M. Croce, “MicroRNAs in Cancer,” *Annu. Rev. Med.*, vol. 60, pp. 167–79, 2009.
- [27] M. Karaman, P. C. Li, and M. O’Donnell, “Synthetic Aperture Imaging for Small Scale Systems,” *IEEE Trans. Ultrason. Ferroelec., Freq. Contr.*, vol. 42, no. 3, pp. 429–442, 1995.
- [28] J. A. Jensen, S. Nikolov, K. L. Gammelmark, and M. H. Pedersen, “Synthetic aperture ultrasound imaging,” *Ultrasonics*, vol. 44, pp. e5–e15, 2006.
- [29] J.-M. Gorce, M. Arditi, and M. Schneider, “Influence of Bubble Size Distribution on the Echogenicity of Ultrasound Contrast Agents - A Study of SonoVue,” *Invest. Radiol.*, vol. 35, no. 11, pp. 661–671, 2000.
- [30] W.-S. Chen, A. A. Brayman, T. J. Matula, and L. A. Crum, “Inertial Cavitation Dose and Hemolysis Produced In Vitro with or without Optison,” *Ultrasound Med. Biol.*, vol. 29, no. 5, pp. 725–737, 2003.
- [31] K. Pu *et al.*, “Semiconducting polymer nanoparticles as photoacoustic molecular imaging probes in living mice,” *Nat. Nanotechnol.*, vol. 9, pp. 233–239, 2014.
- [32] K. J. Livak and T. D. Schmittgen, “Analysis of Relative Gene Expression Data Using Real-Time Quantitative PCR and the 2- $\Delta\Delta$ CT Method,” *Methods*, vol. 25, no. 4, pp. 402–408, Dec. 2001.
- [33] J. Schindelin *et al.*, “Fiji: an open-source platform for biological-image analysis,” *Nat. Methods*, vol. 9, p. 676, Jun. 2012.
- [34] H. Dewitte *et al.*, “Theranostic mRNA-loaded Microbubbles in the Lymphatics of Dogs: {Implications} for Drug Delivery,” *Theranostics*, vol. 5, no. 1, pp. 97–109, 2015.
- [35] Y. Liu, L. Li, Q. Su, T. Liu, Z. Ma, and H. Yang, “Ultrasound-targeted microbubble destruction enhances gene expression of microRNA-21 in swine heart via intracoronary delivery,” *Echocardiography*, vol. 32, pp. 1407–1416, 2015.
- [36] P. C. Lyon *et al.*, “Safety and feasibility of ultrasound-triggered targeted drug delivery of doxorubicin from thermosensitive liposomes in liver tumours (TARDOX): a single-centre, open-label, phase 1 trial,” *Lancet Oncol.*, 2018.